npj | 2D materials and applications

www.nature.com/npj2dmaterials

ARTICLE OPEN

Unveiling the origin of *n*-type doping of natural MoS_2: carbon

Youngsin Park[1,7]✉, Nannan Li[2,7], Daesung Jung[3,7], Laishram Tomba Singh[4,7], Jaeyoon Baik[4], Eunsook Lee[4], Dongseok Oh[4], Young Dok Kim[2], Jin Yong Lee[2], Jeongseok Woo[5], Seungmin Park[5], Hanchul Kim[6], Geunseop Lee[5]✉, Geunsik Lee[1]✉ and Chan-Cuk Hwang[4]✉

MoS_2 has attracted intense interest in many applications. Natural MoS_2 and field-effect transistors made of it generally exhibit *n*-type characteristics, but its origin is unknown. Herein, we show that C is the origin of the universal *n*-type doping of natural MoS_2. Photoemission spectroscopies reveal that while many MoS_2 samples with C detected are *n*-type, some without C exhibit *p*-type characteristics. The C-free, *p*-type MoS_2 changes to *n*-type over time with the concurrent appearance of C that is out-diffused from bulk, indicating that C induces the *n*-type doping. The C-origin is verified by C-deposition and supported by theoretical calculations. This carbon appears as nanometer-scale defects frequently observed in scanning tunneling microscopy. In addition, we propose, based on the calculations, that S vacancies are responsible for the *p*-type characteristics, which contrasts with the widespread belief. This work provides new perspectives on MoS_2 doping and presents a new direction for fabricating reliable MoS_2 devices.

npj 2D Materials and Applications (2023)7:60 ; https://doi.org/10.1038/s41699-023-00424-x

INTRODUCTION

As layered two-dimensional (2D) materials, transition metal dichalcogenides (TMDs) have attracted intense interest owing to their unique properties that are potentially advantageous for applications in wide areas[1–3]. Molybdenum disulfide (MoS_2) is an archetypal TMD material with potential in electronic[4–6], optoelectronic[7,8], photovoltaic[9,10], catalytic[11,12], and sensing[13] applications. Since the successful realization of field-effect transistor (FET) devices using a single or few MoS_2 layer channel[4], considerable research has focused on high-performance and novel electronic and optoelectronic devices using various 2D materials[14–16]. The device performance is affected by intrinsic factors (quality of the materials with defects, including structural imperfections and unintentional impurities) and extrinsic factors (doping from substrates and surface adsorbates, metal-semiconductor junction causing a Schottky barrier). Extensive efforts have been devoted to enhancing the device's performance, focusing mainly on extrinsic factors. Notable progress has been made, for example, through encapsulation[17], dielectric interface engineering[18], and reduction of the Schottky barrier height[19]. It is also important to improve the inherent properties of MoS_2, which are determined by intrinsic factors. As a first step, it is essential to clarify the carrier type and work function (WF) and identify the defects present in natural or grown MoS_2. Such basic knowledge can be exploited to fabricate high-performance devices.

Most MoS_2 FETs exhibit *n*-type transport behavior[4–7,13,20–23], while ambipolar transport was also reported in some studies[24,25]. The band structure of MoS_2 measured using angle-resolved photoemission spectroscopy (ARPES) showed unanimously that the valence band is located well below the Fermi level (E_F) (>1 eV)[26–30]. These have led to the speculation that natural MoS_2 without intentional doping is an *n*-type semiconductor. The intrinsic *n*-type MoS_2 was often attributed to S vacancies, which were believed to be the most abundant and probable defects in MoS_2 owing to its small formation energy[31–34]. On the other hand, the role of S vacancies as electron donors was not supported by most theoretical studies[35–38]. Other impurities, such as Cl or Br[7], Re[36], and H[38], have been suggested as alternative causes of *n*-type doping. Scanning tunneling microscopy (STM) studies have shown that S vacancies and other defects are present near the MoS_2 surfaces[33,39–41]. These near-surface defects were postulated to act as unintended dopants, but their nature has not been identified. Therefore, identifying these intrinsic defects in MoS_2 remains elusive, and a consistent understanding of the origin of the predominantly observed *n*-type properties is lacking.

Here, we present evidence that *n*-type doping of MoS_2 is provided by carbon (C) atoms through studies combining photoemission spectroscopy (PES), STM, and density-functional theory (DFT) calculations. ARPES data have shown that the E_F of the newly exfoliated MoS_2 is located near the valence band maximum (VBM) when C atoms are not detected. As the amount of C increases over time, the E_F gradually moves away from the VBM with a concurrent decrease in the WF, indicating that the C impurity induces a change in doping from *p*- to *n*-type. STM showed that the nanometer-scale defects commonly observed on MoS_2 surfaces increased in number over time, indicating their correlation with C atoms. All these experimental observations correlated to the increasing amounts of C were confirmed by intentionally depositing C atoms on the MoS_2 surface. DFT calculations corroborated the C-induced doping change from *p*- to *n*-type and the WF variation. Theoretical results also suggest that the initial *p*-type doping observed in the absence of carbon is attributed to S vacancies at the surface.

RESULT AND DISCUSSION

Angle-resolved photoemission spectroscopy

Although MoS_2 is one of the representative 2D layered materials, it has a sizable band dispersion (as much as 0.5 eV) in the direction

[1]Department of Chemistry, College of Natural Science, Ulsan National Institute of Science and Technology, Ulsan 44919, Korea. [2]Department of Chemistry, Sungkyunkwan University, Suwon 16419, Korea. [3]Convergence Research Center for Energy and Environmental Science, Sungkyunkwan University, Suwon 16419, Korea. [4]Pohang Accelerator Laboratory, Pohang University of Science and Technology, Pohang 37673, Korea. [5]Department of Physics, Inha University, Incheon 22212, Korea. [6]Department of Applied Physics, Sookmyung Women's University, Seoul 04310, Korea. [7]These authors contributed equally: Youngsin Park, Nannan Li, Daesung Jung, Laishram Tomba Singh.
✉email: ysinpark@unist.ac.kr; glee@inha.ac.kr; gslee@unist.ac.kr; cchwang@postech.ac.kr

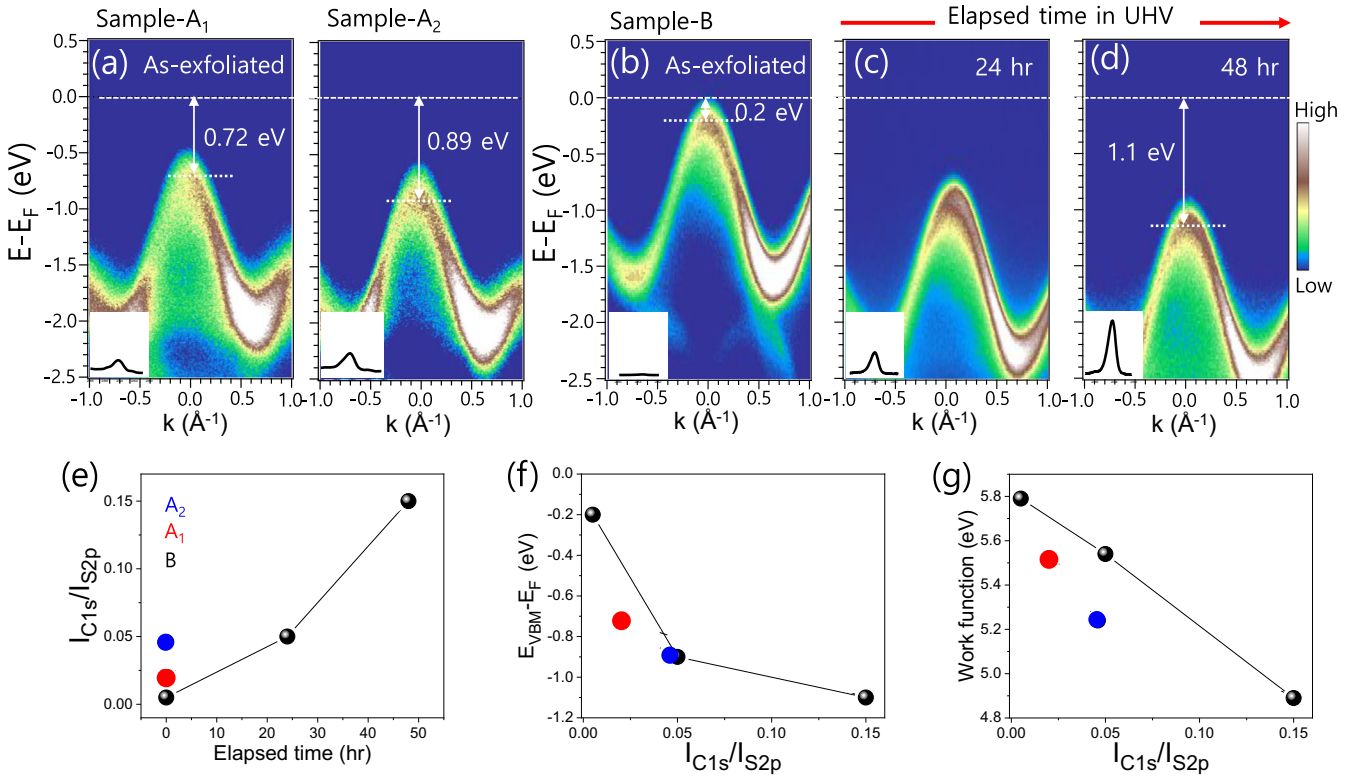

Fig. 1 ARPES and PES spectra with different samples. a ARPES data showing electronic band structures for different MoS_2 samples. Samples-A_1 and A_2 with noticeable amounts of carbon were obtained immediately after exfoliation in the UHV of 1.3×10^{-10} Torr. **b** Another sample-B with a small amount of carbon immediately after exfoliation under UHV, **c** after 24 h, and **d** after 48 h. ARPES data were taken at the photon energy of 56 eV along the Γ-K symmetry direction of the surface Brillouin zone. The color scales in the figures are the same. Insets show C 1s PES spectra corresponding to the ARPES data. **e** Relative peak intensity of C 1s to S 2p (I_{C1s}/I_{S2p}) for samples-A_1, A_2, and B with time. **f** VBM of MoS_2 as a function of I_{C1s}/I_{S2p}. **g** WF of MoS_2 as a function of I_{C1s}/I_{S2p}.

perpendicular to the layers due to interlayer coupling[42]. Therefore, it is crucial to use the appropriate photon energy (56 eV) to determine the VBM accurately when measuring the in-plane band structure (Supplementary Fig. 1). Figure 1a shows experimental band structures measured immediately after exfoliation in ultra-high vacuum (UHV) for representative MoS_2 samples (samples-A_1 and A_2). Many of the investigated samples showed similar data, and overall features (including the VBM at approximately −0.7 to −0.9 eV relative to E_F) are in good agreement with previous results[26–30]. For some freshly exfoliated samples [sample-B in Fig. 1b], ARPES data show rigid energy shifts with a similar band structure to those of Fig. 1a. The exact VBM was determined after taking the constant energy map (Supplementary Fig. 2). The VBM located at −0.2 eV is very close to the E_F, which is very unusual. Considering the bulk band gap of 1.2–1.3 eV, samples-A_1 and A_2 and sample-B are *n*- and *p*-type semiconductors, respectively, exhibiting the variability of MoS_2 in doping. Sample-B, being initially *p*-type, showed a shift of the VBM to higher binding energy (i.e., a shift of E_F upward from the VBM) with time [Fig. 1b–d]. The VBM shifted down by ~0.7 eV after 24 h of aging under UHV without any treatment. After 48 h of aging, the VBM was lowered further, reaching ~−1.1 eV. This indicates that a change in the doping type of the MoS_2 toward *n*-type occurs over time. In order to prove the reproducibility, we tested a number of pristine-MoS_2 samples. About 20–30% of them showed p-type properties, and the others presented n-type properties depending on the carbon amount. In addition to the change in the VBM, the measured WF also changed over time. The WF of sample-B (5.8 eV) was initially larger than those of the freshly exfoliated samples-A_1 and A_2 (WF = 5.2–5.5 eV). However, the WF of sample-B decreased with time and reached 4.9 eV after 48 h, similar to the typical value for the *n*-type MoS_2. High-resolution core-level PES was used to explain the differences in VBM and WF between different MoS_2 samples [insets of Fig. 1a–d and Supplementary Fig. 3]. When the carbon-free sample was kept in the UHV chamber for a long time, the C 1 s peak began to appear and grew slowly over time [insets of Fig. 1c, d, and Supplementary Fig. 3b]. We also investigated the possible adsorption of other adsorbates, such as O_2 and H_2O. Wide spectra taken over time with a photon energy of 630 eV confirm that no other adsorbates are detected except for C (Supplementary Fig. 4).

Figure 1e plots the C_{1s}/S_{2p} peak intensity ratio (I_{C1s}/I_{S2p}) as a function of time for sample-B (data for the as-exfoliated samples-A_1, A_2 are also shown). Figure 1f, g shows the observed VBM and the WF as functions of I_{C1s}/I_{S2p}, respectively. The strong dependence on the carbon content is evident, suggesting that the carbon is responsible for the time-dependent changes in the electronic properties. The correlation of the time-dependent changes in the VBM and the WF to the measured carbon content was well reproduced.

Carbon was deposited directly onto the MoS_2 to clarify the origin of the time-dependent changes shown in Fig. 1. Figure 2a shows the band structure of a MoS_2 containing trace amounts of carbon, where the VBM is very close to the E_F. When carbon was deposited for 5, 10, 15, and 20-min [Fig. 2b–e], the VBM moved down relative to E_F. Finally, the VBM was lowered to −1.18 eV after 20-min deposition. The I_{C1s}/I_{S2p} in Fig. 2f shows that the amount of carbon increased with deposition time. Both the VBM [Fig. 2g] and WF [Fig. 2h] decreased almost linearly with increasing I_{C1s}/I_{S2p}. The results were entirely consistent with the observed aging-induced changes. This shows that carbon is the origin of the changes in the VBM and WF.

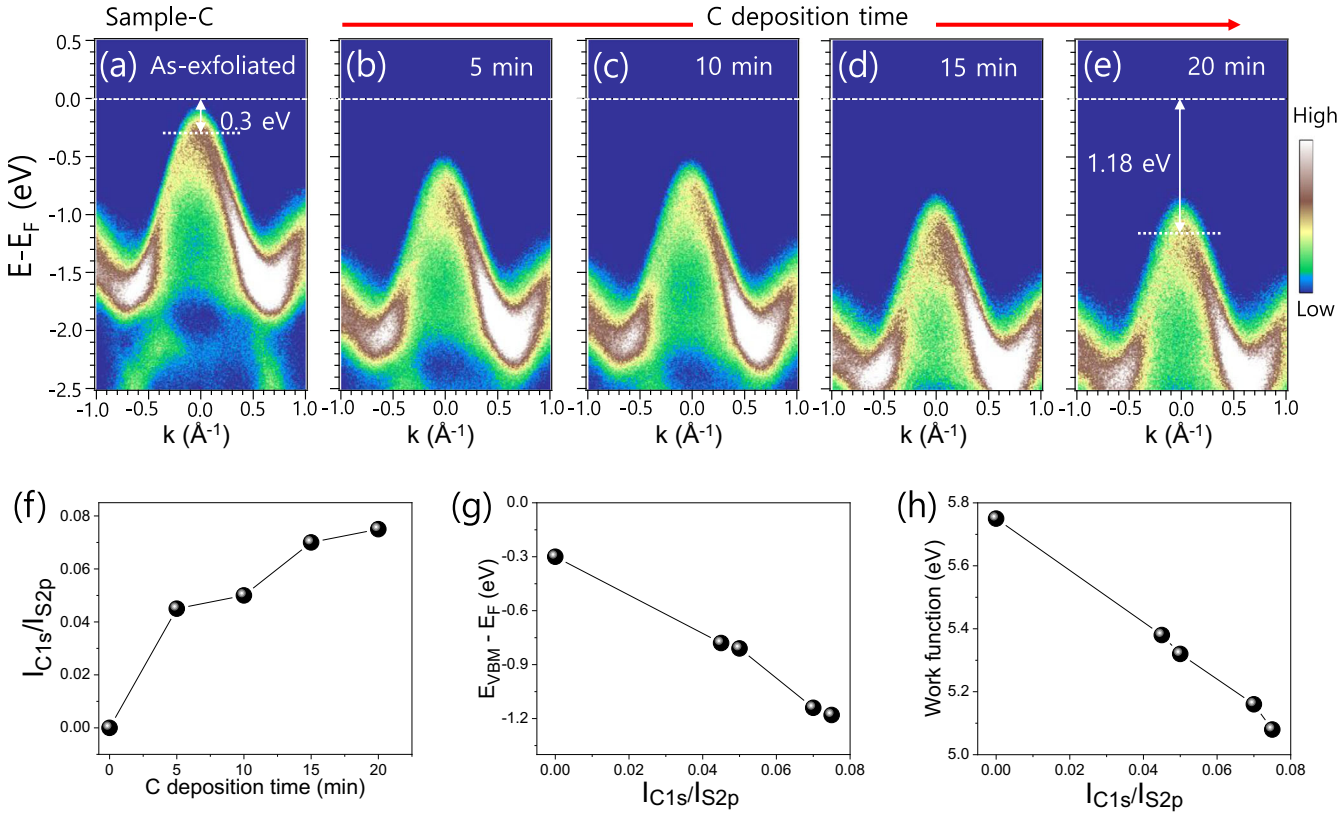

Fig. 2 ARPES with increasing carbon amounts. a–e Evolution of electronic band structures of the as-exfoliated MoS_2 (sample-C) with increasing carbon deposition. **f** I_{C1s}/I_{S2p} as a function of the carbon deposition time. **g** VBM of the MoS_2 as a function of I_{C1s}/I_{S2p}. **h** WF of the MoS_2 as a function of I_{C1s}/I_{S2p}.

Scanning tunneling microscopy

Figure 3 shows STM images of MoS_2. Several point defects are shown in the freshly exfoliated surface [Fig. 3a]. These defects are a few nanometers in size and are distinct from S vacancies that appear on the atomic scale (Supplementary Fig. 5). Two types of nanometer-scale defects could be distinguished at negative sample bias (i.e., in filled-state image): one appearing as bright elevations and the other as dark depressions [inset of Fig. 3b]. Both defects appear dark and are almost indistinguishable at positive sample bias (not shown). These nanometer-scale defects increased in number over time, as shown in a representative image of the MoS_2 surface obtained after 10 days [Fig. 3b]. No other new defects were observed. Previous STM studies also reported observations of these nanometer-scale defects commonly present on MoS_2 surfaces[32–34,39–41]. In some studies, these defects have been attributed to S-vacancies[32,33]. On the other hand, S vacancies were imaged independently as atomic-scale features[40,43] (Supplementary Fig. 6). Thus, the observed nanometer-scale defects cannot be S vacancies, and their origin is still unknown. Considering that the amount of C in the PES data increased with aging, the nanometer-scale defects in STM images could be attributed to C-related features. Therefore, the MoS_2 surface was also investigated after C atoms were deposited to test the C-related origin of the nanometer-scale defects observed in STM images. Figure 3c–e shows the change in the MoS_2 surface with increasing C deposition (deposition time is changed while the other deposition parameters are fixed). The C-deposited surface exhibited the same nanometer-scale defects as those observed on the as-exfoliated and the aged surfaces [inset of Fig. 3d]. No other new defect features were observed. The number of "bright" (B) and "dark" (D) defect features in the filled-state image increased with increasing C deposition time [Fig. 3f], suggesting that both defects are related to C atoms. The consistency between aging and C-deposited samples clearly shows that nanometer-scale defects commonly observed on MoS_2 surfaces originate from C atoms.

In many studies, the almost universal *n*-type characteristics of the MoS_2 materials and transistor devices based on them were attributed to S vacancies. This widely held belief originates from the consideration that the intrinsic S vacancies are prevalent on the surface because of their small formation energy. With the same reasoning, the nanometer-scale defects observed frequently in STM images were often interpreted as S vacancies with one or a few missing S atoms[32–34]. On the other hand, the present study showed that the nanometer-scale defects are clearly distinguished from S vacancies, which is consistent with a recent study[40]. Indeed, those defects are closely related to C impurities.

Density-functional theory calculations

DFT calculations were performed to investigate the origin of the carbon-induced *n*-type doping behavior of MoS_2. In addition to the native S vacancy (V_S), atomic C impurities at the surface were considered, such as the S-substituting C defect (C_S) and the interstitial C defects. Figure 4a shows the local atomic structures around V_S, C_S, and two interstitial C defects (C_{int} and C'_{int}), as well as the pristine (i.e., defect-free) case. C_{int} resembles a CS dimer substituting an S atom, whereas C'_{int} involves a C atom at the hollow site above Mo. C_{int} was found to be the lowest energy structure among all the interstitial defects we considered, which include metastable structures with C residing within the van der Waals (vdW) gap (Supplementary Fig. 6). Figure 4b shows the band structures, where all the energy levels are relative to VBM. The pristine band structure shows an indirect band gap, and the E_F is set to the midgap (0.62 eV above VBM). For V_S, the nearly flat

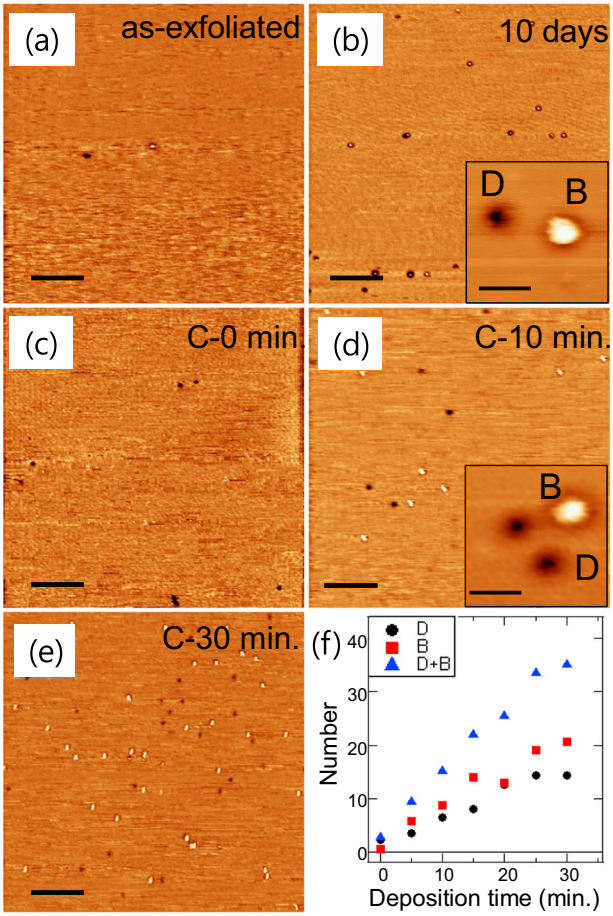

Fig. 3 STM images. STM images of aging effect: as-exfoliated (**a**) and after 10 days of aging (**b**). Effect of C deposition with varying deposition time: 0 min (as-exfoliated) (**c**), 10 min (**d**), and 30 min (**e**). All scale bars are 40 nm in (**a**–**e**), 4 nm for insets of (**b**) and (**d**). **f** The number of defects imaged per frame as a function of the C deposition time. Images were obtained with $V_s = -1.0$ V and $I_t = 0.3$ nA. Insets in (**b**) and (**d**) are zoomed-in images ($V_s = -1.0$ V and $I_t = 0.1$ nA) showing the bright (B) and dark (D) defects. The defects that appeared with aging and after C deposition are the same.

bands (blue symbols) caused by Mo dangling bonds appeared at −0.39 eV (occupied) and 0.81 eV (unoccupied). This shifts the E_F (0.40 eV) closer to VBM compared with the pristine case, which is consistent with the literature[35,36]. Therefore, the MoS_2 surface with V_S exhibits *p*-type characteristics.

In the band structure of a surface with C_S, the dangling bond states of Mo disappear, and an unoccupied C-induced gap state (red symbols) appears at approximately 0.70 eV. Therefore, the E_F is lowered to 0.31 eV, exhibiting *p*-type behavior similar to V_S. For the two interstitial C defects C_{int} (C'_{int}), two C-induced bands appeared: one occupied at ~0.4 (0.6) eV and the other unoccupied at ~1.2 (1.1) eV. The resulting E_F at 0.80 (0.81) eV was raised toward CBM by about 0.18 (0.19) eV, compared with the pristine case. This suggests that both interstitial C defects C_{int} and C'_{int} exhibit *n*-type behavior, which is different from the *p*-type behavior of V_S and C_S defects.

The WFs were calculated for the pristine and the defected MoS_2 surfaces. The WF increased for V_S (5.28 eV) and C_S (5.37 eV) but decreased for C_{int} (4.88 eV) and C'_{int} (4.87 eV) compared to the pristine surface (5.06 eV). The changes in the E_F and the WF due to C_{int} and C'_{int} are consistent with the C-induced changes observed in the ARPES experiments. Therefore, the *p*-type observed for freshly exfoliated MoS_2 is attributed to V_S and possibly to C_S, and the carbon defects causing the *n*-type are ascribed to interstitial C. Two interstitial C (C_{int} and C'_{int}) configurations are matched with the two experimental nanometer-scale defect types (B and D). However, we are not able to match which of the experimental defects corresponds to which theoretical interstitial C configurations due to the limited STM images and the difficulties of simulating such large-size defects.

Based on the theoretical calculations, we propose that S vacancies or S-substituting C atoms induce *p*-type behavior, accounting for the observed E_F close to the VBM [Fig. 1b]. This proposition contradicts the prevailing belief that S vacancies are responsible for *n*-type behavior[31–34]. Whereas the supporting evidence showing that S vacancies induce *p*-type can also be found in previous studies. Several PES studies have reported the change in MoS_2 from *n*- to *p*-type upon thermal annealing[44,45] and ion irradiation[46,47]. Because S vacancies are expected to be generated in those processes, the *n*- to *p*-type change was correlated with S vacancies. Previous STM and scanning tunneling spectroscopy (STS) data obtained near atomic-scale defects, considered neutral S-vacancy defects, showed the E_F close to the VBM, which is indicative of *p*-type. All these previous studies support the proposition that S vacancies (S-substituting C atoms) induce *p*-type properties rather than *n*-type properties. The change from *p*- to *n*-type is due to the near-surface C impurities (interstitial C), which increase in amount over time.

A previous study has reported that as-exfoliated MoS_2 surfaces exhibit almost intrinsic properties, whereas surface electron accumulation (SEA) occurs upon prolonged exposure to air[48]. STS and ARPES data indicated a shift in the E_F toward the conduction band in the aged samples, which is consistent with SEA. The authors attributed the SEA to the formation of S vacancies caused by a slow desulfurization process based on the unsubstantiated correlation between the prevailing *n*-type behavior and the expected predominance of S vacancies. On the other hand, our experimental observations and theoretical calculations clearly show that the change from *p*- to *n*-type is due to near-surface C impurities. Evidently, the C impurities (interstitial C) are the origin of the universally observed *n*-type properties of the MoS_2. Note that there was an older publication reporting a decrease in electron affinity and ionization potential with surface contamination by C[49], which is consistent with the C origin of *n*-type MoS_2 demonstrated in our study.

The remaining question to be answered is where the C impurity atoms originate. The C impurity was recently reported for another TMD, WS_2 monolayer synthesized by chemical vapor deposition (CVD)[50,51]. In those studies, CH substituting for S atoms (CH_S) was proposed as the most stable C-related point defect on monolayer WS_2 in the plasma-enhanced CVD environment with methane gas. The possibility of the external origin of the C-related impurities on our MoS_2 from residual C-containing molecules in UHV was tested by dosing C_2H_2 and CO gases. Despite the significant amounts of dosing, C_2H_2 resulted in no changes in the band structure, whereas CO induced a slight downward shift of the VBM. However, the change was too small to account for the temporal changes (Supplementary Fig. 7). Note that the CH_S defects on monolayer WS_2 show similar nanometer-scale STM contrast to the B defects on MoS_2[51]. CH incorporation is a possible high-temperature process in hydrocarbon-containing environments, but since our experiments were not carried out in such environments, we rule out the possibility of the CH_S as C-related defects on MoS_2.

Our DFT calculations show that carbon atoms favor near-surface regions (Supplementary Fig. 8), so there exists a net thermodynamic driving force for outward C diffusion. The inner C atoms will diffuse mainly along paths whose energy barriers are relatively lower than others. We speculate the diffusion path consisting of (1) horizontal hoppings from one C_{int} site to neighboring C_{int} sites

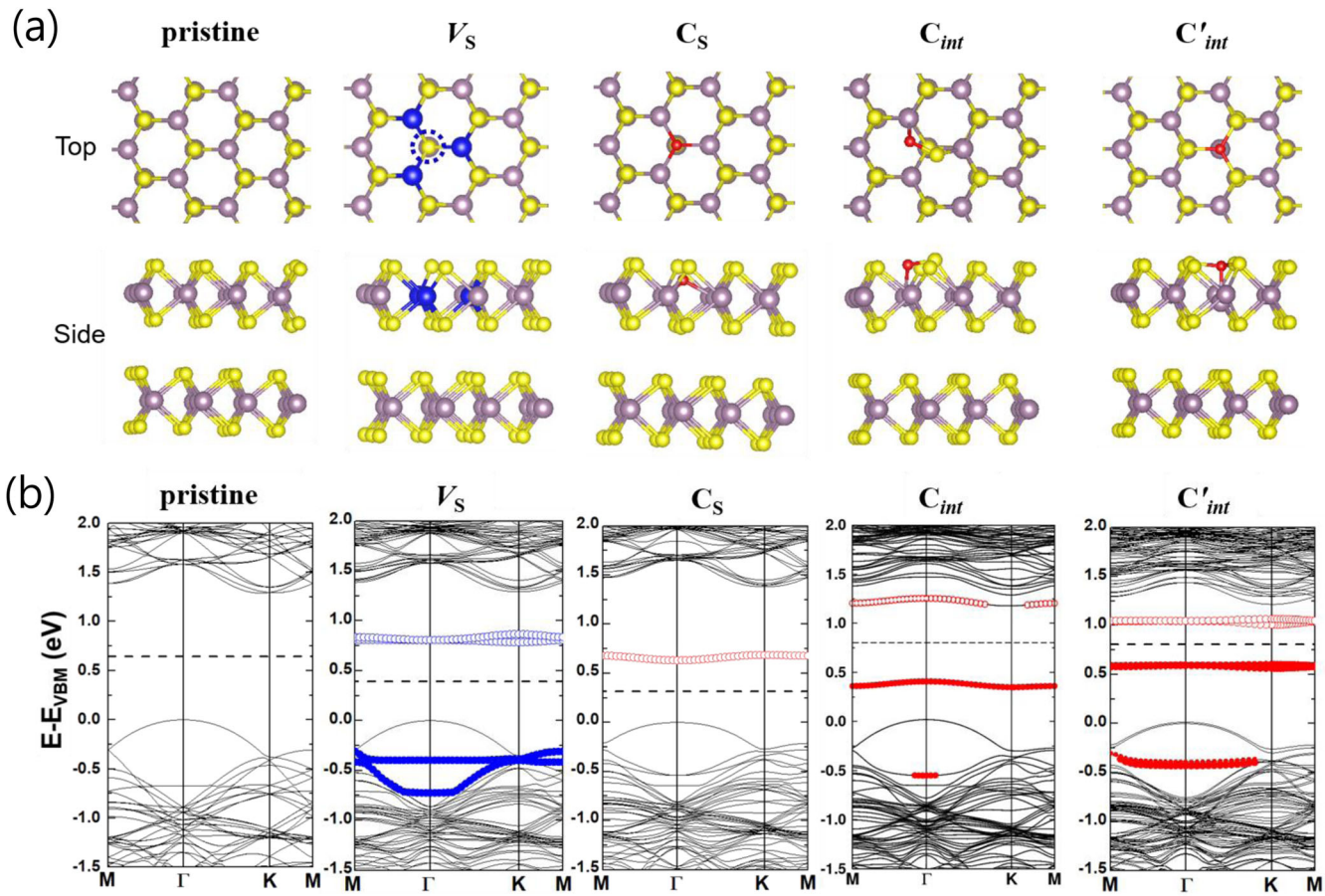

Fig. 4 DFT calculations. a Top and side views of pristine MoS_2, defective ones with S vacancy (V_S), S-substituting C defect (C_S), and two interstitial C defects (C_{int} and C'_{int}). Atomic defects are located at the outermost atomic layer. The bright purple, yellow, and red balls denote the Mo, S, and C atoms, respectively, while the three blue balls are Mo atoms adjacent to V_S (indicated by the dashed circle). **b** Band structures of pristine and defective MoS_2 bilayers using a 4×4 supercell. The horizontal dashed line indicates the E_F set to be the center of the energy gap. The blue and red circles denote the major contributions of Mo atoms with the dangling bonds and C atoms, respectively. The solid and open circles indicate the occupied and unoccupied states, respectively. All the energy levels are aligned relative to the VBM for easy recognition of the E_F shift.

via C'_{int}, (2) vertical hoppings across vdW gaps, and (3) penetrations through atomic (MoS_2) layers. Our calculations of hopping barriers suggest that the vertical hopping across the vdW gap is much slower than the horizontal hopping (Supplementary Fig. 9). While C impurities hardly go through complete MoS_2 layers, they will be able to cross each MoS_2 layer through sufficiently large voids. Since chemically active sites around voids are more likely to be passivated, the associated penetration of C atoms is expected to be relatively easy. Therefore, we estimate the outward diffusion length to be of the order of sub-micrometer per one day at room temperature (RT) (see Supplementary Note 8). It matches reasonably well with the experimental time scale to observe an increased amount of C atoms.

The C atoms can exist in different configurations, C_{int} (or C'_{int}) and C_S, when the MoS_2 sample contains V_S defects. The calculated formation energies of considered defects indicate that a C_S defect is more stable by 4.5 eV than coexisting single defects of V_S and C_{int}. This implies that C impurity atoms tend to form C_S defects by occupying the existing S vacancies. As discussed above, C impurity atoms would diffuse outward over time after exfoliation, whose form is likely to be C_{int} and change to C_S by sitting down to V_S near the surface at an early stage. The electronic band structure indicates that C_S, like V_S, exhibits *p*-type characteristics, which is in accordance with the observed *p*-type ARPES data for freshly exfoliated samples. Over time, all existing S vacancies are consumed. Then, additional out-diffusing C atoms inevitably constitute the less stable C_{int} defects that exhibit *n*-type properties. This is consistent with the ARPES observations of changes from *p*-type to *n*-type with aging. We also confirmed that the stable charge states are neutral in the significant portion of the range of E_F for all the considered defects (Supplementary Fig. 10).

A question remains whether the carbon can be the origin of the *n*-type conductivity even in MoS_2 FETs where monolayer and/or CVD-grown samples are used, and thus C diffusion from bulk is excluded. In these cases, we speculate that C impurities may be incorporated during or after synthesis in the process of transfer for the measurement or device fabrication.

In summary, we have shown that C atoms near the surface of MoS_2 are responsible for the predominant *n*-type doping of natural minerals and the frequently observed nanometer-scale defects at the surface in STM images. Newly exfoliated MoS_2 surfaces occasionally exhibit *p*-type behavior when C atoms are barely detected. The *p*-type MoS_2 is due to S vacancies at the surface. The carbon-free *p*-type MoS_2 changes to *n*-type over time with the simultaneous increase in the amounts of C. The carbon atoms are supposed to migrate from the bulk to the near-surface region, resulting in unintentional *n*-type doping of the MoS_2 surface. The origin of the intrinsic *p*- and *n*-type doping of natural MoS_2 disclosed in this study provides new prospects to control doping for electronic and optoelectronic applications.

METHODS

Photoemission spectroscopy

Experiments were conducted using commercially available single-crystal 2H-MoS_2 flakes, referred to as "pristine MoS_2." The pristine MoS_2 crystals were exfoliated using the scotch-tape method in ultra-high vacuum (UHV) with pressures ranging from 10^{-8} to 10^{-10} Torr. After transferring the exfoliated sample to the analysis chamber, The PES data were measured at the 10D beamline of the Pohang Accelerator Laboratory (PAL), which is equipped with Scienta DA30, R4000, and PHOIBOS 150 analyzers. For the exfoliated surface, the valence band and the C 1s and O 1s core levels were measured. A photon energy of 56 eV was used for the valence band and WF measurements, and 360 and 650 eV for C 1s and O 1s peaks, respectively. The binding energies were calibrated by measuring the Au Fermi energy or Au $4f_{7/2}$ core-level peak depending on the photon energy. A bias voltage of −10 V with an uncertainty of ±0.01 V was applied to the samples for the WF measurements. All the photoemission data were collected at RT. A homemade C evaporator, where an electron beam hits a carbon rod (99.99%), was used for carbon deposition in the PES experiments.

Scanning tunneling microscopy

STM experiments were carried out in an independent UHV chamber with a base pressure $<3.0 \times 10^{-10}$ Torr. For the experiments, single-crystal flakes of natural MoS_2 minerals mounted on pieces of a Si wafer were exfoliated using scotch tape in the UHV for in-situ measurements. The STM measurements were performed at RT using two STM instruments: a home-built STM and a commercial STM (SPECS Inc.). All STM images were taken in the constant current mode. The same e-beam C evaporator as in the PES experiments was used for carbon deposition in the STM experiments.

Density-functional theory calculations

Theoretical calculations were performed within the Vienna Ab-initio Simulation Package (VASP)[52]. The projector-augmented-wave pseudopotentials were used for the plane wave basis set for modeling the ion cores. The Perdew–Burke–Ernzerhof generalized gradient approximation was used for the exchange-correlation functional with the inclusion of spin polarization. The optB88-vdW van der Waals density-functional was used to describe the dispersion interactions in each system. A kinetic energy cutoff of 500 eV for the basis set and a $5 \times 5 \times 1$ k-point mesh for the Brillouin zone integration were used for the 4×4 MoS_2 bilayer supercell. All atomic structures were fully relaxed until the forces on each atom were less than 0.01 eV/Å.

DATA AVAILABILITY

The data of this study are available from the corresponding author upon reasonable request.

Received: 13 March 2023; Accepted: 28 August 2023;
Published online: 05 September 2023

REFERENCES

1. Wang, Q. H., Kalantar-Zadeh, K., Kis, A., Coleman, J. N. & Strano, M. S. Electronics and optoelectronics of two-dimensional transition metal dichalcogenides. *Nat. Nanotechnol.* **7**, 699–712 (2012).
2. Schmidt, H., Giustiniano, F. & Eda, G. Electronic transport properties of transition metal dichalcogenide field-effect devices: surface and interface effects. *Chem. Soc. Rev.* **44**, 7715–7736 (2015).
3. Manzeli, S., Ovchinnikov, D., Pasquier, D., Yazyev, O. V. & Kis, A. 2D transition metal dichalcogenides. *Nat. Rev. Mater.* **2**, 17033 (2017).
4. Radisavljevic, B., Radenovic, A., Brivio, J., Giacometti, V. & Kis, A. Single-layer MoS_2 transistors. *Nat. Nanotechnol.* **6**, 147–150 (2011).
5. Kim, S. et al. High-mobility and low-power thin-film transistors based on multi-layer MoS_2 crystals. *Nat. Commun.* **3**, 1011 (2012).
6. Schmidt, H. et al. Transport properties of monolayer MoS_2 grown by chemical vapor deposition. *Nano Lett.* **14**, 1909–1913 (2014).
7. Yin, Z. et al. Single-layer MoS_2 phototransistors. *ACS Nano* **6**, 74–80 (2012).
8. Mak, K. F. et al. Tightly bound trions in monolayer MoS_2. *Nat. Mater.* **12**, 207–211 (2013).
9. Bernardi, M., Palummo, M. & Grossman, J. C. Extraordinary sunlight absorption and one nanometer thick photovoltaics using two-dimensional monolayer materials. *Nano Lett.* **13**, 36643670 (2013).
10. Wi, S. et al. Enhancement of photovoltaic response in multilayer MoS_2 induced by plasma doping. *ACS Nano* **8**, 5270–5281 (2014).
11. Zong, X. et al. Photocatalytic H_2 evolution on MoS_2/CdS catalysts under visible light irradiation. *J. Phys. Chem. C* **114**, 1963–1968 (2010).
12. Lukowski, M. A. et al. Enhanced hydrogen evolution catalysis from chemically exfoliated metallic MoS_2 nanosheets. *J. Am. Chem. Soc.* **135**, 10274–10277 (2013).
13. Li, H. et al. Fabrication of single- and multilayer MoS_2 film-based FET for sensing NO at RT. *Small* **8**, 63–67 (2012).
14. Bhimanapati, G. R. et al. Recent advances in two-dimensional materials beyond graphene. *ACS Nano* **9**, 11509–11539 (2015).
15. Wang, F. et al. Progress on electronic and optoelectronic devices of 2D layered semiconducting materials. *Small* **13**, 1604298 (2017).
16. Li, S. et al. p-/n-Type modulation of 2D transition metal dichalcogenides for electronic and optoelectronic devices. *Nano Res.* **15**, 123–144 (2022).
17. Lee, G. H. et al. Highly stable, dual-gated MoS_2 transistors encapsulated by hexagonal boron nitride with gate-controllable contact, resistance, and threshold voltage. *ACS Nano* **9**, 7019–7026 (2015).
18. Zou, X. et al. Dielectric engineering of a boron nitride/hafnium oxide hetero-structure for high-performance 2D field effect transistors. *Adv. Mater.* **28**, 2062–2069 (2016).
19. Liu, Y. et al. Approaching the Schottky-Mott limit in van der Waals metal-semiconductor junctions. *Nature* **557**, 696–700 (2018).
20. Lee, Y. H. et al. Synthesis of large-area MoS_2 atomic layers with chemical vapor deposition. *Adv. Mater.* **24**, 2320–2325 (2012).
21. Liu, K. K. et al. Growth of large-area and highly crystalline MoS_2 thin layers on insulating substrates. *Nano Lett.* **12**, 1538–1544 (2012).
22. Baugher, B. W. H., Churchill, H. O. H., Yang, Y. & Jarillo-Herrero, P. Intrinsic electronic transport properties of high-quality monolayer and bilayer MoS_2. *Nano Lett.* **13**, 4212–4216 (2013).
23. Ahn, J. H., Parkin, W. M., Naylor, C. H., Johnson, A. T. C. & Drndić, M. Ambient effects on electrical characteristics of CVD-grown monolayer MoS_2 field-effect transistors. *Sci. Rep.* **7**, 4075 (2017).
24. Zhang, Y., Ye, J., Matsuhashi, Y. & Iwasa, Y. Ambipolar MoS_2 thin flake transistors. *Nano Lett.* **12**, 1136–1140 (2012).
25. Bao, W., Cai, X., Kim, D., Sridhara, K. & Fuhrer, M. S. High mobility ambipolar MoS_2 field-effect transistors: substrate and dielectric effects. *Appl. Phys. Lett.* **102**, 042104 (2013).
26. Han, S. W. et al. Band-gap expansion in the surface-localized electronic structure of MoS_2(0002). *Phys. Rev. B* **86**, 115105 (2012).
27. Jin, W. et al. Osgood, Direct measurement of the thickness-dependent electronic band structure of MoS_2 using angle-resolved photoemission spectroscopy. *Phys. Rev. Lett.* **111**, 106801 (2013).
28. Alidoust, N. et al. Observation of monolayer valence band spin-orbit effect and induced quantum well states in MoX_2. *Nat. Commun.* **5**, 4673 (2014).
29. Miwa, J. A. et al. Electronic structure of epitaxial single-layer MoS_2. *Phys. Rev. Lett.* **114**, 046802 (2015).
30. Latzke, D. K. et al. Electronic structure, spin-orbit coupling, and interlayer interaction in bulk MoS_2 and WS_2. *Phys. Rev. B* **91**, 235202 (2015).
31. Qiu, H. et al. Hopping transport through defect-induced localized states in molybdenum disulphide. *Nat. Commun.* **4**, 2642 (2013).
32. McDonnell, S., Addou, R., Buie, C., Wallace, R. M. & Hinkle, C. L. Defect-dominated doping and contact resistance in MoS_2. *ACS Nano* **8**, 2880–2888 (2014).
33. Lu, C. P., Li, G., Mao, J., Wang, L. M. & Andrei, E. Y. Bandgap, mid-gap states, and gating effects in MoS_2. *Nano Lett.* **14**, 4628–4633 (2014).
34. Park, J. H. et al. Defect passivation of transition metal dichalcogenides via a charge transfer van der Waals interface. *Sci. Adv.* **3**, e1701661 (2017).
35. Noh, J. Y., Kim, H. & Kim, Y. S. Stability and electronic structures of native defects in single-layer MoS_2. *Phys. Rev. B* **89**, 205417 (2014).
36. Komsa, H. P. & Krasheninnikov, A. V. Native defects in bulk and monolayer MoS_2 from first principles. *Phys. Rev. B* **91**, 125304 (2015).
37. Pandey, M. et al. Defect-tolerant monolayer transition metal dichalcogenides. *Nano Lett.* **16**, 2234–2239 (2016).

38. Singh, A. & Singh, A. K. Origin of n-type conductivity of monolayer MoS_2. *Phys. Rev. B* **99**, 121201 (2019). (R).
39. Addou, R., Colombo, L. & Wallace, R. M. Surface defects on natural MoS_2. *ACS Appl. Mater. Interfaces* **7**, 11921–11929 (2015).
40. Bampoulis, P. et al. Defect dominated charge transport and Fermi level pinning in MoS_2/metal contacts. *ACS Appl. Mater. Interfaces* **9**, 19278–19286 (2017).
41. Liu, X., Balla, I., Bergeron, H. & Hersam, M. C. Point defects and grain boundaries in rotationally commensurate MoS_2 on epitaxial graphene. *J. Phys. Chem. C* **120**, 20798–20805 (2016).
42. Böker, T. et al. Band structure of MoS_2, $MoSe_2$, and a-$MoTe_2$: angle-resolved photoelectron spectroscopy and ab initio calculations. *Phys. Rev. B* **64**, 235305 (2001).
43. Vancsó, P. et al. The intrinsic defect structure of exfoliated MoS_2 single layers revealed by scanning tunneling microscopy. *Sci. Rep.* **6**, 29726 (2016).
44. Donarelli, M., Bisti, F., Perrozzi, F. & Ottaviano, L. Tunable sulfur desorption in exfoliated MoS_2 by means of thermal annealing in ultra-high vacuum. *Chem. Phys. Lett.* **588**, 198–202 (2013).
45. Zhang, X. et al. Unravelling the effect of sulfur vacancies on the electronic structure of the MoS_2 crystal. *Phys. Chem. Chem. Phys.* **22**, 21776–21783 (2020).
46. Chen, Y. et al. Tuning electronic structure of single layer MoS_2 through defect and interface engineering. *ACS Nano* **12**, 2569 (2018).
47. Bussolotti, F., Yang, J., Kawai, H., Wong, C. P. Y. & Goh, K. E. J. Impact of S-vacancies on the charge injection barrier at the electrical contact with the MoS_2 monolayer. *ACS Nano* **15**, 2686–2579 (2021).
48. Siao, M. D. et al. Two-dimensional electronic transport and surface electron accumulation in MoS_2. *Nat. Commun.* **9**, 1442 (2018).
49. McGovern, I. T., Williams, R. H. & Mee, C. H. B. Electronic properties of cleaved molybdenum disulphide surfaces. *Surf. Sci.* **46**, 427–440 (1974).
50. Zhang, F. et al. Carbon doping of WS_2 monolayers: bandgap reduction and *p*-type doping transport. *Sci. Adv.* **5**, eaav5003 (2019).
51. Cochrane, K. et al. Intentional carbon doping reveals CH as an abundant charged impurity in nominally undoped synthetic WS_2 and WSe_2. *2D Mater.* **7**, 031003 (2020).
52. Kresse, G. & Furthmuller, J. Efficient iterative schemes for ab initio total-energy calculations using a plane-wave basis set. *Phys. Rev. B* **54**, 11169 (1996).

ACKNOWLEDGEMENTS

This research was supported by the Basic Science Research Program (2021R1A2C1006113, 2020R1A2B5B02001876, 2021R1A2C1006039 and 2020R1A2C2013757), Nano·Material Technology Development Program (2021M3H4A1A02055667), and the Creative Materials Discovery Program (2020M3D1A1110548) through the National Research Foundation of Korea (NRF) funded by Ministry of Science and ICT. This work was supported by the National Supercomputing Center with supercomputing resources, including technical support (No. KSC-2021-CRE-0258, KSC-2021-CRE-0567, KSC-2021-CRE-0574, KSC-2022-CRE-0497). The experiments at PLS were supported in part by the Ministry of Science and ICT and POSTECH.

AUTHOR CONTRIBUTIONS

Y.P., D.J., L.T.S., J.B., E.L., D.O., Y.D.K., C.C.H. performed the ARPES experiments. J.W., S.P., and G.L. performed the STM experiments. N.L., J.Y.L., H.K., and G.S.L. performed the DFT calculations. C.C.H., G.S.L., and G.L. supervised the project.

COMPETING INTERESTS

The authors declare no competing interests.

ADDITIONAL INFORMATION

Supplementary information The online version contains supplementary material available at https://doi.org/10.1038/s41699-023-00424-x.

Correspondence and requests for materials should be addressed to Youngsin Park, Geunseop Lee, Geunsik Lee or Chan-Cuk Hwang.